



UNIVERSITY OF LEEDS

This is a repository copy of *Spatial Chirp-based Joint Optimization for Analog Beamforming in Reconfigurable Intelligent Surface Assisted Terahertz Ultra-wideband Systems*.

White Rose Research Online URL for this paper:

<https://eprints.whiterose.ac.uk/id/eprint/229496/>

Version: Accepted Version

---

**Proceedings Paper:**

Chen, X., Zhang, L. [orcid.org/0000-0002-4535-3200](https://orcid.org/0000-0002-4535-3200), Fan, P. et al. (2 more authors) (Accepted: 2025) Spatial Chirp-based Joint Optimization for Analog Beamforming in Reconfigurable Intelligent Surface Assisted Terahertz Ultra-wideband Systems. In: 2025 IEEE Vehicular Technology Conference (VTC2025-Fall). 2025 IEEE 102nd Vehicular Technology Conference: VTC2025-Fall, 19-22 Oct 2025, Chengdu, China. IEEE (In Press)

---

This is an author produced version of an conference paper accepted for publication in 2025 IEEE Vehicular Technology Conference (VTC2025-Fall), made available under the of the Creative Commons Attribution License (CC-BY), which permits unrestricted use, distribution and reproduction in any medium, provided the original work is properly cited.

**Reuse**

This article is distributed under the terms of the Creative Commons Attribution (CC BY) licence. This licence allows you to distribute, remix, tweak, and build upon the work, even commercially, as long as you credit the authors for the original work. More information and the full terms of the licence here: <https://creativecommons.org/licenses/>

**Takedown**

If you consider content in White Rose Research Online to be in breach of UK law, please notify us by emailing [eprints@whiterose.ac.uk](mailto:eprints@whiterose.ac.uk) including the URL of the record and the reason for the withdrawal request.



[eprints@whiterose.ac.uk](mailto:eprints@whiterose.ac.uk)  
<https://eprints.whiterose.ac.uk/>

# Spatial Chirp-based Joint Optimization for Analog Beamforming in Reconfigurable Intelligent Surface Assisted Terahertz Ultra-wideband Systems

Xingyu Chen, Li Zhang

*School of Electronic & Electrical Eng  
University of Leeds  
Leeds, UK*

{el18x2c, l.x.zhang}@leeds.ac.uk

Pingzhi Fan

*Institute of Mobile Communications  
Southwest Jiaotong University  
Chengdu, China*

pzfan@swjtu.edu.cn

Ke Chen, Yejing Fan

*School of Electronic & Electrical Eng  
University of Leeds  
Leeds, UK*

{ml20k2c, el17yf}@leeds.ac.uk

**Abstract**—This paper proposes a spatial chirp-based joint optimization method for analog beamforming in RIS-assisted THz ultra-wideband communication systems. The THz band (0.1-10 THz) offers significantly wider bandwidth, enabling Tbps data rates, which are crucial for 6G communications. However, traditional phase shifters are optimized for a single frequency. In ultra-wideband systems, the phase response deviates as frequency varies, leading to beam squinting problem, which significantly degrades system performance. Existing solutions, such as true-time-delay architectures, impose excessive complexity, making them impractical for THz systems. In this work, we propose leveraging polynomial expansion to optimize the spatially dependent phase functions of RIS, Tx, and Rx. We formulate the optimization problem as maximizing system throughput, and develop a gradient ascent-based iterative algorithm to solve it. Simulation results demonstrate that our method outperforms conventional and state-of-the-art approaches in metrics including phase response, throughput, and BER, providing a cost-effective solution for optimizing analog beamforming.

**Index Terms**—analog beamforming, reconfigurable intelligent surface, terahertz, ultra-wideband, joint optimization.

## I. INTRODUCTION

Terahertz (THz) ultra-wideband (UWB) communications represent a pivotal frontier for 5G and beyond wireless networks, offering the potential to meet unprecedented bandwidth demands while overcoming the spectrum limitations faced by current technologies. The THz band (0.1 to 10 THz) provides vastly broader bandwidth, potentially spanning hundreds of gigahertz (GHz). This enables data rates that can reach terabits per second (Tbps), which is essential for emerging applications such as holographic communications, digital twins, and extended reality [1]. Furthermore, THz communications facilitate extremely low latency ( $< 1$  ms) and higher connection density (up to  $10^7$  devices per  $\text{km}^2$ ), aligning with 6G requirements for enhanced mobile broadband, massive machine-type communications, and ultra-reliable low-latency communications [2]. Despite challenges including propagation losses and hardware limitations, research indicates that integrating THz technologies with advanced techniques such as extremely large-scale antenna arrays (ELAA) and reconfigurable intelligent surfaces

(RIS) could unlock the transformative potential of future networks [3].

RIS represents a paradigm-shifting technology for THz communications, functioning as programmable electromagnetic structures that can dynamically manipulate incident wavefronts through controlled phase shifters. These phase shifters are independently configurable to alter their electromagnetic properties, thereby enabling real-time modification of the wireless propagation environment [2]. In THz communications, RIS technology offers a compelling solution by establishing virtual line-of-sight (LoS) links around obstacles and extending coverage to non-LoS (nLoS) regions, effectively increasing network connectivity by up to 40% in dense urban environments [4]. Furthermore, RIS deployments can substantially mitigate the distance-dependent path loss characteristic of THz frequencies, potentially improving received signal power by 15 to 20 dB [5]. Recent advancements in low-loss, high-efficiency THz metamaterials have significantly enhanced RIS feasibility for practical THz systems. These advancements, combined with energy-efficient control mechanisms, position RIS as a crucial enabler for reliable, ultra-high-speed THz communication networks [6].

In addition, analog beamforming represents a cornerstone technology for THz communications, primarily due to the severe path loss and atmospheric absorption challenges inherent to this frequency band [7]. By employing ELAA and RIS, along with precisely optimized phase shifters, analog beamforming enables the concentration of electromagnetic energy into narrow directional beams, effectively mitigating propagation losses [8]. This approach is especially beneficial for THz systems where digital processing of UWB signals would lead to prohibitive power consumption and hardware complexity. Recent advancements in RIS have further enhanced efficiency of analog beamforming, enabling dynamic beam steering with reduced implementation complexity compared to conventional phase array structures [9].

However, analog beamforming in THz UWB communications faces substantial challenges, with beam squinting emerging as a particularly significant obstacle. As traditional phase

shifters are optimized for a single frequency, in the ultra-wide bandwidth of THz systems, the phase response deviates as frequency varies, leading to beam squinting problem [10]. The severity of beam squinting increases proportionally with bandwidth, becoming especially problematic in THz UWB systems, causing substantial signal degradation and throughput reduction at the bandwidth edges. Conventional mitigation strategies, such as true-time-delay (TTD) architectures, provide theoretical solutions. However, they introduce prohibitive hardware complexity, insertion losses, and higher power consumption, especially when scaled to the massive antenna arrays needed for THz communications [1]. Practical and cost-effective solutions for THz UWB systems remain elusive.

In this work, we propose a spatial chirp-based joint optimization method for analog beamforming in RIS-aided THz UWB systems where transmitters (Tx) and receivers (Rx) are equipped with phased uniform planar arrays (UPA). The core idea behind using spatial chirp is to determine phase shifters through a spatially dependent phase function, which is algorithm-driven, offering a low-cost solution to analog beamforming in THz UWB systems. This concept was initially introduced in [11] to broaden beams in far-field narrowband scenarios using an empirical approach. The authors in [12] applied this approach in phased Tx circular planar array (CPA) systems to achieve uniform equivalent wideband channel response. Recently, its application was expanded to RIS-aided single Tx and Rx antenna systems [13].

However, to the best of our knowledge, no existing work has used spatial chirp to optimize analog beamforming in RIS-assisted phased Tx and Rx UPA systems. We define the optimization problem as maximizing system throughput, and use polynomial expansion to approximate the optimal phase functions for RIS, Tx, and Rx. In this way, the maximization variables are defined by polynomial coefficients, making the optimization problem solvable. To solve the maximization problem, an iterative algorithm based on gradient ascent is designed. We evaluate the performance of the proposed method through simulation results. The results demonstrate its improvement over conventional narrowband beamforming [14] and the state-of-the-art minimum mean square error (MMSE) based wideband beamforming method [15]. The improvements are measured in terms of signal-to-noise ratio (SNR), throughput, and bit error rate (BER).

## II. SYSTEM AND CHANNEL MODELS

We focus on an indoor RIS-assisted THz UWB downlink communication system, where RIS, Tx, and Rx are analog phased square UPA equipped with  $N_S$ ,  $N_T$ , and  $N_R$  elements/antennas, respectively. We consider the use of orthogonal frequency division multiplexing (OFDM) in the system with bandwidth  $BW$ , central frequency  $f_c$ , and number of subcarriers  $S_c$ , where the sub-bands are evenly distributed. Denote  $f_m$  as the frequency for the  $m^{\text{th}}$  ( $m = 1, 2, \dots, S_c$ ) subcarrier, then  $f_m = f_c - \frac{BW}{2} + \frac{BW}{S_c}(m - \frac{1}{2})$ . All antennas are isotropic with unit gains, and their spacing is set to  $\frac{\lambda}{2}$ , where  $\lambda = \frac{c}{f_c}$  is the wavelength at  $f_c$ , and  $c$  is the speed

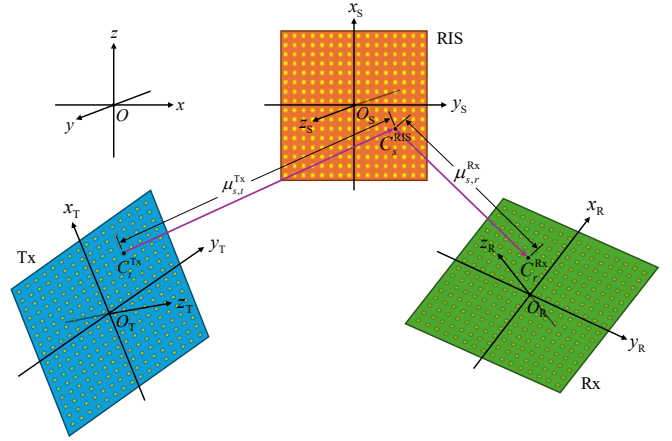


Fig. 1. System model of RIS, Tx, and Rx UPA.

of light. The side lengths of RIS, Tx, and Rx UPA are  $L_S = \frac{\lambda}{2}\sqrt{N_S}$ ,  $L_T = \frac{\lambda}{2}\sqrt{N_T}$ , and  $L_R = \frac{\lambda}{2}\sqrt{N_R}$ , respectively. We assume that the locations and orientations of the Tx, Rx, and RIS are known using technologies such as near-field channel estimation and localization algorithms.

### A. System Model

RIS, Tx, and Rx are illustrated in Fig. 1 by orange, blue, and green UPA, respectively, where elements/antennas are represented by the golden sequins. The global coordinate system is defined by  $x$ -,  $y$ -, and  $z$ -axes, with the origin at  $O = (0, 0, 0)$ . The local coordinate systems for RIS, Tx, and Rx are determined by  $x_S$ -,  $y_S$ -, and  $z_S$ -axes,  $x_T$ -,  $y_T$ -, and  $z_T$ -axes, and  $x_R$ -,  $y_R$ -, and  $z_R$ -axes, with the origins  $O_S$ ,  $O_T$ , and  $O_R$ , respectively. Denote the global coordinates of the  $s^{\text{th}}$  ( $s = 1, 2, \dots, N_S$ ) RIS element, the  $t^{\text{th}}$  ( $t = 1, 2, \dots, N_T$ ) Tx antenna, and the  $r^{\text{th}}$  ( $r = 1, 2, \dots, N_R$ ) Rx antenna as  $G_s^{\text{RIS}}$ ,  $G_t^{\text{Tx}}$ , and  $G_r^{\text{Rx}}$ , respectively, while denoting their local coordinates as  $C_s^{\text{RIS}}$ ,  $C_t^{\text{Tx}}$ , and  $C_r^{\text{Rx}}$ , respectively. In this way,  $C_s^{\text{RIS}} = (x_{s_p}, y_{s_q}, 0)$ , where  $x_{s_p}$  ( $y_{s_q}$ ) is the local discrete spatial variable of RIS, and  $s_p$  ( $s_q$ ) =  $1, 2, \dots, \sqrt{N_S}$  is the row(column) index of the  $s^{\text{th}}$  RIS element satisfying  $s = s_p + (s_q - 1)\sqrt{N_S}$ . Similarly,  $C_t^{\text{Tx}} = (x_{t_p}, y_{t_q}, 0)$ , where  $t_p$  ( $t_q$ ) =  $1, 2, \dots, \sqrt{N_T}$ ,  $t = t_p + (t_q - 1)\sqrt{N_T}$ , and  $C_r^{\text{Rx}} = (x_{r_p}, y_{r_q}, 0)$ , where  $r_p$  ( $r_q$ ) =  $1, 2, \dots, \sqrt{N_R}$ ,  $r = r_p + (r_q - 1)\sqrt{N_R}$ . Since the spacing of elements/antennas is  $\frac{\lambda}{2}$ , we have  $x_{s_p} = \frac{\lambda}{2}(s_p - \frac{1}{2}) - \frac{L_S}{2}$ ,  $y_{s_q} = \frac{\lambda}{2}(s_q - \frac{1}{2}) - \frac{L_S}{2}$ ,  $x_{t_p} = \frac{\lambda}{2}(t_p - \frac{1}{2}) - \frac{L_T}{2}$ ,  $y_{t_q} = \frac{\lambda}{2}(t_q - \frac{1}{2}) - \frac{L_T}{2}$ ,  $x_{r_p} = \frac{\lambda}{2}(r_p - \frac{1}{2}) - \frac{L_R}{2}$ , and  $y_{r_q} = \frac{\lambda}{2}(r_q - \frac{1}{2}) - \frac{L_R}{2}$ .

The global array coordinates can be derived from the local array coordinates based on the origin and orientation of the UPA. For example, the local coordinate system of RIS undergoes right-handed rotations of  $\theta_x$ ,  $\theta_y$ , and  $\theta_z$  around the global  $x$ -,  $y$ -, and  $z$ -axes, respectively. Thus, the corresponding coordinate transformation matrices for the rotations, denoted as  $\mathbf{T}_x$ ,  $\mathbf{T}_y$ , and  $\mathbf{T}_z$ , are

$$\mathbf{T}_x = \begin{bmatrix} 1 & 0 & 0 \\ 0 & \cos(\theta_x) & \sin(\theta_x) \\ 0 & -\sin(\theta_x) & \cos(\theta_x) \end{bmatrix}, \quad (1)$$

$$\mathbf{T}_y = \begin{bmatrix} \cos(\theta_y) & 0 & \sin(\theta_y) \\ 0 & 1 & 0 \\ -\sin(\theta_y) & 0 & \cos(\theta_y) \end{bmatrix}, \quad (2)$$

$$\mathbf{T}_z = \begin{bmatrix} \cos(\theta_z) & \sin(\theta_z) & 0 \\ -\sin(\theta_z) & \cos(\theta_z) & 0 \\ 0 & 0 & 1 \end{bmatrix}, \quad (3)$$

and

$$\vec{G}_s^{\text{RIS}} = \vec{O}_S + \mathbf{T}_z \mathbf{T}_y \mathbf{T}_x \vec{C}_s^{\text{RIS}}, \quad (4)$$

where  $\vec{C}$  denotes the vector pointing to coordinate  $C$ .

### B. Channel Model

We consider static LoS channels between Tx and RIS, as well as between RIS and Rx, since they dominate over nLoS channels [16]. Additionally, we assume that the LoS channel between Tx and Rx is blocked, as is common in most RIS-aided systems research. The wideband channel matrices for the Tx-RIS and RIS-Rx channels, denoted as  $\mathbf{H}_T(f_m)$  and  $\mathbf{H}_R(f_m)$ , are determined by the corresponding geometry-based static LoS channel transfer functions (CTF) [17],  $h_{s,t}^{\text{Tx}}(f_m) \in \mathbb{C}$  and  $h_{r,s}^{\text{Rx}}(f_m) \in \mathbb{C}$ , as

$$\mathbf{H}_T(f_m) = [h_{s,t}^{\text{Tx}}(f_m)]_{N_S \times N_T}, \quad (5)$$

$$\mathbf{H}_R(f_m) = [h_{r,s}^{\text{Rx}}(f_m)]_{N_R \times N_S}, \quad (6)$$

where

$$h_{s,t}^{\text{Tx}}(f_m) = \frac{c}{4\pi f_m \mu_{s,t}^{\text{Tx}}} e^{-j \frac{2\pi f_m \mu_{s,t}^{\text{Tx}}}{c}}, \quad (7)$$

$$h_{r,s}^{\text{Rx}}(f_m) = \frac{c}{4\pi f_m \mu_{r,s}^{\text{Rx}}} e^{-j \frac{2\pi f_m \mu_{r,s}^{\text{Rx}}}{c}}, \quad (8)$$

where  $\mu_{s,t}^{\text{Tx}}$  is the signal propagation distance between the  $s^{\text{th}}$  RIS element and the  $t^{\text{th}}$  Tx antenna, given by  $\mu_{s,t}^{\text{Tx}} = \|\vec{G}_s^{\text{RIS}} - \vec{G}_t^{\text{Tx}}\|$ , and  $\mu_{r,s}^{\text{Rx}}$  is the distance between the  $r^{\text{th}}$  Rx antenna and the  $s^{\text{th}}$  RIS element, given by  $\mu_{r,s}^{\text{Rx}} = \|\vec{G}_r^{\text{Rx}} - \vec{G}_s^{\text{RIS}}\|$ .

The beamformers for the RIS, Tx, and Rx, denoted as  $\vec{B}_S$ ,  $\vec{B}_T$ , and  $\vec{B}_R$ , are given by phase sequences  $\phi_s^{\text{RIS}}$ ,  $\phi_t^{\text{Tx}}$ , and  $\phi_r^{\text{Rx}}$  with  $\vec{B}_S = [\text{diag}\{\phi_s^{\text{RIS}}\}]_{N_S \times N_S}$ ,  $\vec{B}_T = [\phi_t^{\text{Tx}}]_{N_T \times 1}$ , and  $\vec{B}_R = [\phi_r^{\text{Rx}}]_{N_R \times 1}$ , respectively, where the operation  $\text{diag}\{\cdot\}$  denotes placing element at diagonal. The phase sequences are determined by spatially dependent phase functions for the RIS, Tx, and Rx, denoted as  $\varphi_S$ ,  $\varphi_T$ , and  $\varphi_R$ , respectively, that

$$\phi_s^{\text{RIS}} = e^{j\varphi_S(x_{sp}, y_{sq})}, \quad (9)$$

$$\phi_t^{\text{Tx}} = e^{j\varphi_T(x_{tp}, y_{tq})}, \quad (10)$$

$$\phi_r^{\text{Rx}} = e^{j\varphi_R(x_{rp}, y_{rq})}. \quad (11)$$

The equivalent channel gain, denoted as  $g(f_m)$ , is given by

$$g(f_m) = \vec{B}_R^H \mathbf{H}_R(f_m) \vec{B}_S \mathbf{H}_T(f_m) \vec{B}_T. \quad (12)$$

## III. JOINT OPTIMIZATION METHOD

In this section, we first define the optimization problem and then develop an algorithm tailored to efficiently solve it. The optimization problem is formulated as maximizing system throughput, where the optimization variables are transformed from phase functions to polynomial coefficients to make the problem tractable. The optimization algorithm iteratively updates the polynomial coefficients using gradient ascent method with dynamic step size to achieve maximum throughput.

### A. Optimization Problem Formulation

The optimization variables are the spatially dependent phase functions  $\varphi_S$ ,  $\varphi_T$ , and  $\varphi_R$ . Once they are optimized, the phase sequences for RIS, Tx, and Rx are determined according to (9), (10), and (11), respectively. We aim to maximize the system throughput during the optimization, which means the optimal phase functions, denoted as  $\hat{\varphi}_S$ ,  $\hat{\varphi}_T$ , and  $\hat{\varphi}_R$ , correspond to the maximum throughput. The throughput of the OFDM system, denoted as  $TP$ , is calculated by SNR of the subcarriers,  $SNR(f_m)$ , as [18]

$$TP = \frac{BW}{S_c} \sum_{m=1}^{S_c} \log_2(1 + SNR(f_m)), \quad (13)$$

$$SNR(f_m) = \frac{\rho |g(f_m)|^2}{\sigma(f_m) N_T N_R BW}, \quad (14)$$

where  $\rho$  is total input power that can be determined by users, e.g.,  $\rho = 0$  dBm for indoor THz transmissions, and  $\sigma(f_m)$  is the thermal noise spectral power density at  $f_m$  [18].

According to (12),  $TP$  is a function of  $\varphi_S$ ,  $\varphi_T$ , and  $\varphi_R$ . Thereby, the optimization problem can be stated as

$$(\hat{\varphi}_S, \hat{\varphi}_T, \hat{\varphi}_R) = \max_{\varphi_S, \varphi_T, \varphi_R} \arg TP. \quad (15)$$

As shown above, the optimization variables are functions, making the maximization problem difficult to solve. Therefore, we use polynomial expansions to construct  $\varphi_S$ ,  $\varphi_T$ , and  $\varphi_R$  as

$$\varphi_S(x, y) = \sum_{v=1}^u \sum_{w=0}^v \varepsilon_{k_{v,w}}^{\text{RIS}} x^{v-w} y^w, \quad (16)$$

$$\varphi_T(x, y) = \sum_{v=1}^u \sum_{w=0}^v \varepsilon_{k_{v,w}}^{\text{Tx}} x^{v-w} y^w, \quad (17)$$

$$\varphi_R(x, y) = \sum_{v=1}^u \sum_{w=0}^v \varepsilon_{k_{v,w}}^{\text{Rx}} x^{v-w} y^w, \quad (18)$$

where  $u$  is the degree of the polynomial, and  $\varepsilon_{k_{v,w}}$  is the coefficient of the  $k_{v,w}^{\text{th}}$  term satisfying  $k_{v,w} = \frac{v^2+v}{2} + w$ . The number of polynomial terms, denoted as  $U$ , is given by  $U = \max(k_{v,w}) = \frac{u^2+3u}{2}$ . Since  $\varphi_S$ ,  $\varphi_T$ , and  $\varphi_R$  have finite spatial domains, it can be effectively constructed by the polynomial with finite  $u$ . Consequently,  $TP$  is now a function of the coefficient vector  $\vec{\varepsilon}$ , defined as

$$\vec{\varepsilon} = \left[ \left[ \varepsilon_{k_{v,w}}^{\text{RIS}} \right]_{U \times 1}^T, \left[ \varepsilon_{k_{v,w}}^{\text{Tx}} \right]_{U \times 1}^T, \left[ \varepsilon_{k_{v,w}}^{\text{Rx}} \right]_{U \times 1}^T \right]_{3U \times 1}^T. \quad (19)$$

Thereby,  $\hat{\varphi}_S$ ,  $\hat{\varphi}_T$ , and  $\hat{\varphi}_R$  can be calculated by optimized  $\vec{\varepsilon}$ , denoted as  $\vec{\varepsilon}^*$ , and the optimization problem is reformulated as

$$\hat{\varepsilon} = \max_{\vec{\varepsilon}} \arg TP. \quad (20)$$

### B. Optimization Algorithm

To solve the optimization problem in (20), we design an iterative algorithm based on gradient ascent. The gradients of  $TP$  in the  $i^{\text{th}}$  ( $i = 1, 2, \dots, I$ ) iteration, where  $I$  is the maximum number of iterations, is given by partial derivatives as

$$\nabla TP[i] = \left[ \frac{\partial TP[i]}{\partial \vec{\varepsilon}[i]} \right]_{3U \times 1}. \quad (21)$$

When calculating  $\nabla TP$  computationally, e.g.,  $\frac{\partial TP}{\partial \varepsilon_1^{\text{RIS}}}$ , a minimal increment is added to  $\varepsilon_1^{\text{RIS}}$ , and the corresponding increment of  $TP$  is calculated by (16), (9), (12), (14), and (13), sequentially. The partial derivative is then obtained as  $\frac{\Delta TP}{\Delta \varepsilon_1^{\text{RIS}}}$ .

Once derived  $\nabla TP[i]$ ,  $\vec{\varepsilon}$  is updated in the next iteration by

$$\vec{\varepsilon}[i+1] = \vec{\varepsilon}[i] + \text{sign}\{\nabla TP[i]\} \odot \vec{S}[i], \quad (22)$$

where  $\text{sign}\{\cdot\}$  denotes pointwise sign function that  $\text{sign}\{x\} = \frac{x}{|x|}$ ,  $\odot$  denotes pointwise multiplication, and  $\vec{S} = [S_k]_{3U \times 1}$  is the step size vector. In this way,  $\vec{\varepsilon}$  always tracks the positive directions of  $\nabla TP$  during the iterations.

To adjust the convergence speed, we define dynamic  $\vec{S}$  that when  $i > 1$ ,  $S_k[i]$  will stretch by a factor  $\tau$  if the  $k^{\text{th}}$  gradient keeps the same sign compared to the last iteration, or shrink to half if not. That is

$$\begin{cases} S_k[i] = \tau S_k[i-1], \Gamma_k[i] > 0 \\ S_k[i] = \frac{1}{2} S_k[i-1], \Gamma_k[i] \leq 0 \end{cases}, \quad (23)$$

where  $[\Gamma_k[i]]_{3U \times 1} = \nabla TP[i] \odot \nabla TP[i-1]$ . When  $i = 1$ , we set  $\vec{S}[i] = [1]_{3U \times 1}$ .

The convergence speed can be adjusted by changing  $\tau$ . To obtain fast and complete convergence, usually  $U$  is set to 2,  $\tau$  is set between 1.5 and 1.7, and  $I$  is set between 40 and 50, which will be discussed further in Section IV-A. In this way, step size will keep stretching if direction of the gradient remains unchanged during the tracking. If the direction inverts, indicating that the maximum value occurs between the last two steps, the step size will be halved to approach it. Since  $\tau < 2$ ,  $\vec{S}$  will turn to zeros while  $TP$  approaches to maximum.

### C. Optimization Initialization

The optimization algorithm needs an appropriate initialization in the first iteration. It can be determined by low-complexity sub-optimal solutions, e.g., the conventional far-field narrowband analog beamforming solutions [14]. They can be adapted in our system model designed at  $f_c$ , denoted as  $\tilde{\varphi}_S$ ,  $\tilde{\varphi}_T$ , and  $\tilde{\varphi}_R$  for the phase functions of RIS, Tx, and Rx, respectively, and given by channel angular information as

$$\begin{aligned} \tilde{\varphi}_S(x, y) = & \frac{2\pi f_c}{c} [(\cos(\alpha_x^{\text{RIS}}) - \cos(\beta_x^{\text{RIS}}))x \\ & + (\cos(\alpha_y^{\text{RIS}}) - \cos(\beta_y^{\text{RIS}}))y], \end{aligned} \quad (24)$$

$$\tilde{\varphi}_T(x, y) = -\frac{2\pi f_c}{c} (\cos(\beta_x^{\text{Tx}})x + \cos(\beta_y^{\text{Tx}})y), \quad (25)$$

$$\tilde{\varphi}_R(x, y) = -\frac{2\pi f_c}{c} (\cos(\alpha_x^{\text{Rx}})x + \cos(\alpha_y^{\text{Rx}})y), \quad (26)$$

where  $\alpha_x^{\text{RIS}}/\beta_x^{\text{RIS}}$  is the angle between arrived/departed signal ray at RIS center and  $x_S$ -axis, defined as the  $x_S$ -based angle of arrival/departure (AoA/AoD) of RIS, and  $\alpha_y^{\text{RIS}}/\beta_y^{\text{RIS}}$  is the angle between that and  $y_S$ -axis, defined as the  $y_S$ -based AoA/AoD of RIS. Similarly,  $\beta_x^{\text{Tx}}/\beta_y^{\text{Tx}}$  is the  $x_T$ -/ $y_T$ -based AoD of Tx, and  $\alpha_x^{\text{Rx}}/\alpha_y^{\text{Rx}}$  are the  $x_R$ -/ $y_R$ -based AoA of Rx.

These angles can be calculated using coordinate operation. For example, to calculate  $\alpha_x^{\text{RIS}}$ , we first get the vector of the arrived signal ray from Tx center to RIS center, i.e.,  $r\vec{a}_y = \vec{O}_S - \vec{O}_T$ . Next, we obtain the vector of the  $x_S$ -axis according to (4), i.e.,  $\vec{x}_S = \vec{O}_S + \mathbf{T}_z \mathbf{T}_y \mathbf{T}_x [1, 0, 0]^T$ . Then,  $\alpha_x^{\text{RIS}}$  is given by  $\cos^{-1}(\frac{\vec{x}_S^T r\vec{a}_y}{\|\vec{x}_S\| \|r\vec{a}_y\|})$ .

Compared to (16), (17), and (18),  $\tilde{\varphi}_S$ ,  $\tilde{\varphi}_T$ , and  $\tilde{\varphi}_R$  actually only contain the first degree of the polynomial, with the higher-degree coefficients set to zero. Therefore,  $\vec{\varepsilon}$  can be initialized with  $\tilde{\varphi}_S$ ,  $\tilde{\varphi}_T$ , and  $\tilde{\varphi}_R$  in the first iteration by setting

$$\vec{\varepsilon}[1] = \frac{2\pi f_c}{c} \begin{bmatrix} \cos(\alpha_x^{\text{RIS}}) - \cos(\beta_x^{\text{RIS}}) \\ \cos(\alpha_y^{\text{RIS}}) - \cos(\beta_y^{\text{RIS}}) \\ [0]_{(U-2) \times 1} \\ -\cos(\beta_x^{\text{Tx}}) \\ -\cos(\beta_y^{\text{Tx}}) \\ [0]_{(U-2) \times 1} \\ -\cos(\alpha_x^{\text{Rx}}) \\ -\cos(\alpha_y^{\text{Rx}}) \\ [0]_{(U-2) \times 1} \end{bmatrix}_{3U \times 1}. \quad (27)$$

The complete optimization algorithm is described below.

---

#### Algorithm 1: Joint Optimization of RIS, Tx, and Rx

---

**Input:**  $\mathbf{H}_T(f_m)$ ,  $\mathbf{H}_R(f_m)$ ,  $U$ ,  $I$ ,  $\tau$

**Output:**  $\vec{B}_S$ ,  $\vec{B}_T$ ,  $\vec{B}_R$

- 1 Set  $i = 1$ ;
  - 2 Set  $\vec{\varepsilon}[i]$  by (27);
  - 3 Set  $\vec{S}[i] = [1]_{3U \times 1}$ ;
  - 4 **while**  $i \leq I$  **do**
    - 5 Calculate  $\nabla TP[i]$  by Equation (21);
    - 6 **if**  $i > 1$  **then**
      - 7 | Update  $\vec{S}[i]$  by Equation (23);
    - 8 **end**
    - 9 **if**  $i < I$  **then**
      - 10 |  $i = i + 1$ ;
      - 11 | Update  $\vec{\varepsilon}[i]$  by Equation (22);
    - 12 **end**
  - 13 **end**
  - 14 Calculate  $\hat{\varphi}_S(x_{s_p}, y_{s_q})$ ,  $\hat{\varphi}_T(x_{t_p}, y_{t_q})$ , and  $\hat{\varphi}_R(x_{r_p}, y_{r_q})$  using  $\vec{\varepsilon}[i]$  by (16), (17), and (18), respectively;
  - 15 Calculate  $\vec{B}_S$ ,  $\vec{B}_T$ , and  $\vec{B}_R$  by (9), (10), and (11), respectively;
-

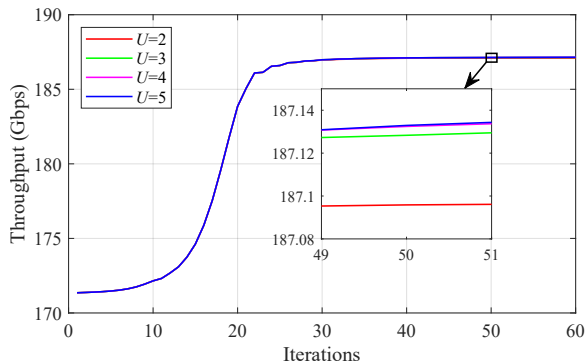


Fig. 2. Throughput during iterations with different values of  $U$ , simulated with  $\tau = 1.5$  and  $I = 60$ .

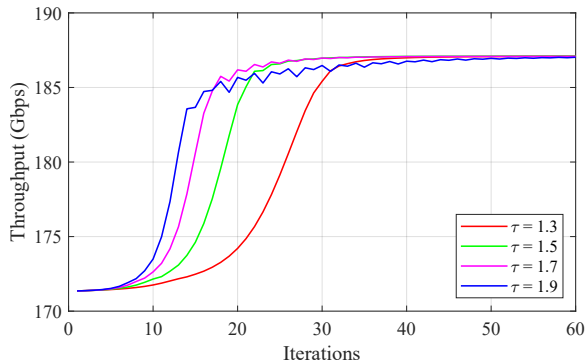


Fig. 3. Throughput during iterations with different values of  $\tau$ , simulated with  $U = 2$  and  $I = 60$ .

#### IV. SIMULATION RESULTS

In this section, we evaluate the proposed optimization method by simulation using MatLab R2022b. To ensure that the optimization algorithm performs efficiently, the algorithmic performance, including convergence behavior under varying algorithm parameters, is presented and analyzed to provide recommended parameter values for optimal performance. Finally, the performance in terms of SNR, throughput, and BER, is presented to demonstrate the effectiveness of the proposed optimization method. Except for the conventional method [14], the results are compared to the state-of-the-art MMSE-based wideband beamforming method [15], where  $\vec{B}_T$  and  $\vec{B}_R$  are derived from their optimized fully digital beamformers using the eigen-beamforming method in [19].

An indoor scenario with a space of  $5\text{ m} \times 5\text{ m} \times 3\text{ m}$  is considered in the simulation. Tx is fixed at  $O_T = (0, 2.5, 2.5)$  with orientations of  $(\theta_x, \theta_y, \theta_z) = (0, -\frac{\pi}{2}, 0)$ . RIS is fixed at  $O_S = (0.5, 2.5, 3)$  with orientations of  $(\theta_x, \theta_y, \theta_z) = (0, 0, 0)$ . Rx is randomly located with  $\{O_R \in \mathbb{R}^3 | x \in [0, 5], y \in [0, 5], z \in [0, 2]\}$  and randomly oriented with  $(\theta_x, \theta_y, \theta_z) \in [-\pi, \pi]$ . We consider THz UWB downlink communication with  $f_c = 300\text{ GHz}$ ,  $BW = 30\text{ GHz}$ , and  $S_c = 256$ . We set  $N_S = 64 \times 64$ ,  $N_T = 32 \times 32$ , and  $N_R = 16 \times 16$  for the RIS, Tx, and Rx UPA, respectively. We assume  $\rho = 0\text{ dBm}$ , and  $\sigma(f_m)$  is calculated at a room temperature of  $290\text{ K}$  as in [18]. BER is obtained using quadrature phase shift keying

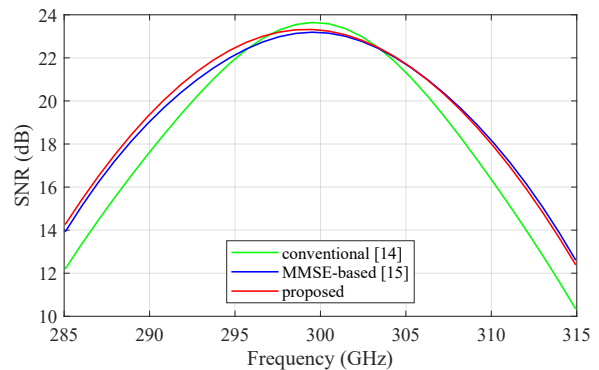


Fig. 4. SNR in the frequency band, simulated with  $\rho = 0\text{ dBm}$ .

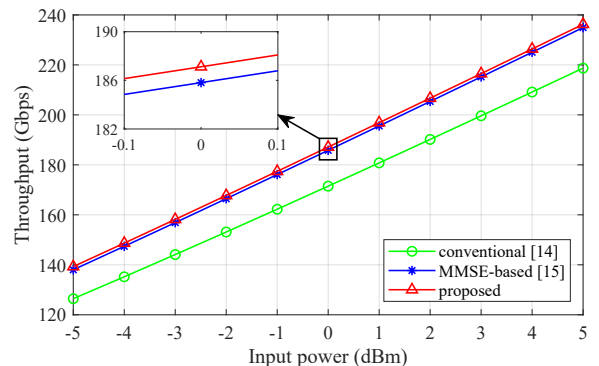


Fig. 5. Throughput versus input power.

(QPSK) modulation. Each result is based on the average of 3000 randomly generated Rx locations.

##### A. Algorithm Performance

The parameter  $U$  determines the polynomial degree, as well as the size of  $\vec{\varepsilon}$ . Theoretically, the optimal phase function can be more accurately approached with a larger  $U$ , but in practice, it is not feasible, as computational complexity increases significantly with  $U$ . Hence, a suitable value of  $U$  is crucial to the efficiency of the optimization algorithm. To demonstrate the influence of  $U$  on the optimization, Fig. 2 shows throughput in different iterations with different values of  $U$ . As shown, a larger value of  $U$  does not lead to significant improvement in throughput, where the slight difference is highlighted by the sub-figure. However, the ratio of average runtime for  $U = 2, 3, 4, 5$  is  $1 : 1.41 : 1.83 : 2.29$ . Therefore,  $U = 2$  is recommended in the consideration of algorithmic efficiency.

To present the influence of  $\tau$  on the optimization, Fig. 3 plots throughput in different iterations with different values of  $\tau$ . As shown, for  $\tau = 1.3$  and  $\tau = 1.5$ , their convergences are steadier while slower than that of  $\tau = 1.7$  and  $\tau = 1.9$  in the early stages of iterations. For  $\tau = 1.9$ , the convergence becomes unstable with oscillation that hinders the maximization process. Based on these results, to achieve fast and complete convergence, it is recommended to set  $\tau$  between 1.5 and 1.7, and  $I$  between 40 and 50.

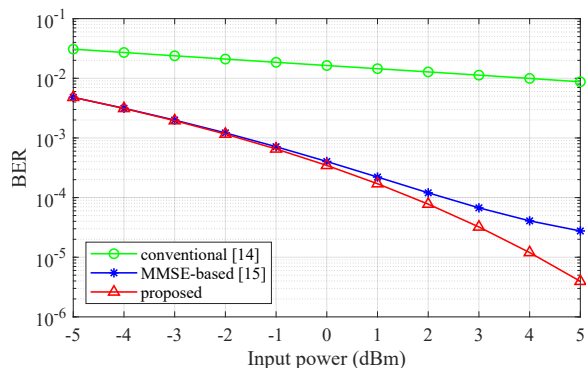


Fig. 6. BER versus input power.

## B. System Performance

We use  $U = 2$ ,  $\tau = 1.5$ , and  $I = 50$  for the simulations in this part. To demonstrate the effectiveness of optimization on phase response, Fig. 4 shows the value of  $SNR(f_m)$  in the frequency band. As shown, the optimal solution couples with a more uniform spectrum of SNR compared to the conventional solution, providing an anti-fading effect for phase response near the band edges. This result indicates that the proposed optimization method can effectively suppress the beam squinting problem of analog beamforming in THz UWB communications.

To illustrate the impact of optimization on system performance, Fig. 5 shows the throughput versus input power, while Fig. 6 presents its corresponding BER. From these figures, it is clear that the proposed optimal solution provides improved throughput and reduced BER compared to that of the conventional and MMSE-based solutions, where the effect of reducing BER appears significant as the input power increases, validating the effectiveness of the proposed optimization method.

## V. CONCLUSION

This paper focuses on analog beamforming in RIS-assisted THz UWB communication systems, where a spatial chirp-based joint optimization method for phase shifters of RIS, Tx, and Rx UPA is proposed. The method is evaluated in terms of phase response, throughput, and BER through simulations in an indoor scenario. The effectiveness of the method is demonstrated through comparisons with the conventional and state-of-the-art analog beamforming approaches, where the proposed optimal solutions achieve the highest throughput and the lowest BER. Moreover, our method characterizes phase functions by polynomial coefficients, and iteratively optimizes these coefficients rather than massive phase sequences. In the aspect of computational complexity, it is more promising for RIS-aided ELAA systems. Despite the high-complexity introduced by iterations, we are committed to reducing it to make the algorithm more efficient. Significant progress has been made by leveraging singular value decomposition (SVD) and feedforward neural network (FNN).

## REFERENCES

- [1] W. Saad, M. Bennis, and M. Chen, "A vision of 6g wireless systems: Applications, trends, technologies, and open research problems," *IEEE Network*, vol. 34, no. 3, pp. 134–142, 2020.
- [2] H. Tataria, M. Shafi, A. F. Molisch, M. Dohler, H. Sjöland, and F. Tufvesson, "6g wireless systems: Vision, requirements, challenges, insights, and opportunities," *Proceedings of the IEEE*, vol. 109, no. 7, pp. 1166–1199, 2021.
- [3] M. Giordani, M. Polese, M. Mezzavilla, S. Rangan, and M. Zorzi, "Toward 6g networks: Use cases and technologies," *IEEE Communications Magazine*, vol. 58, no. 3, pp. 55–61, 2020.
- [4] C. Chaccour, M. N. Soorki, W. Saad, M. Bennis, and P. Popovski, "Can terahertz provide high-rate reliable low-latency communications for wireless vr?" *IEEE Internet of Things Journal*, vol. 9, no. 12, pp. 9712–9729, 2022.
- [5] B. Ning, Z. Chen, W. Chen, and Y. Du, "Channel estimation and transmission for intelligent reflecting surface assisted thz communications," in *ICC 2020 - 2020 IEEE International Conference on Communications (ICC)*, 2020, pp. 1–7.
- [6] I. F. Akyildiz, C. Han, Z. Hu, S. Nie, and J. M. Jornet, "Terahertz band communication: An old problem revisited and research directions for the next decade," *IEEE Transactions on Communications*, vol. 70, no. 6, pp. 4250–4285, 2022.
- [7] C. Han, A. O. Bicen, and I. F. Akyildiz, "Multi-wideband waveform design for distance-adaptive wireless communications in the terahertz band," *IEEE Transactions on Signal Processing*, vol. 64, no. 4, pp. 910–922, 2016.
- [8] T. S. Rappaport, Y. Xing, G. R. MacCartney, A. F. Molisch, E. Mellios, and J. Zhang, "Overview of millimeter wave communications for fifth-generation (5g) wireless networks—with a focus on propagation models," *IEEE Transactions on Antennas and Propagation*, vol. 65, no. 12, pp. 6213–6230, 2017.
- [9] B. Ning, Z. Chen, W. Chen, Y. Du, and J. Fang, "Terahertz multi-user massive mimo with intelligent reflecting surface: Beam training and hybrid beamforming," *IEEE Transactions on Vehicular Technology*, vol. 70, no. 2, pp. 1376–1393, 2021.
- [10] C. Han, A. O. Bicen, and I. F. Akyildiz, "Multi-ray channel modeling and wideband characterization for wireless communications in the terahertz band," *IEEE Transactions on Wireless Communications*, vol. 14, no. 5, pp. 2402–2412, 2015.
- [11] K. H. Sayidmarie and Q. H. Sultan, "Synthesis of wide beam array patterns using quadratic-phase excitations," *Int. J. Electromagn. Appl.*, vol. 3, no. 6, p. 127–135, 2013.
- [12] N. J. Myers and R. W. Heath, "Infocus: A spatial coding technique to mitigate misfocus in near-field los beamforming," *IEEE Transactions on Wireless Communications*, vol. 21, no. 4, pp. 2193–2209, Apr. 2022.
- [13] Z. Huang, R. Prüller, S. Schwarz, and M. Rupp, "Misfocus-reduction in ris-assisted ultra-wideband wireless communication," in *2023 Joint European Conference on Networks and Communications 6G Summit (EuCNC/6G Summit)*, 2023, pp. 108–113.
- [14] B. Ning, W. Mei, L. Zhu, Z. Chen, and R. Zhang, "Max-min beamformer for thz wideband communications," in *2023 IEEE International Conference on Communications Workshops (ICC Workshops)*, 2023, pp. 1747–1752.
- [15] X. Chen, P. Raj Gautam, and L. Zhang, "Low-complexity phase shifter design for reconfigurable intelligent surface aided mmwave massive mimo systems," in *2024 IEEE Wireless Communications and Networking Conference (WCNC)*, 2024, pp. 1–6.
- [16] Y. Xie, B. Ning, L. Li, and Z. Chen, "Near-field beam training in thz communications: The merits of uniform circular array," *IEEE Wireless Communications Letters*, vol. 12, no. 4, pp. 575–579, 2023.
- [17] J. Wang, C.-X. Wang, J. Huang, H. Wang, X. Gao, X. You, and Y. Hao, "A novel 3d non-stationary gbsm for 6g thz ultra-massive mimo wireless systems," *IEEE Transactions on Vehicular Technology*, vol. 70, no. 12, pp. 12 312–12 324, 2021.
- [18] A. Moldovan, M. A. Ruder, I. F. Akyildiz, and W. H. Gerstacker, "Los and nlos channel modeling for terahertz wireless communication with scattered rays," in *2014 IEEE Globecom Workshops (GC Wkshps)*, 2014, pp. 388–392.
- [19] C. Fonteneau, M. Crussière, and B. Jahan, "An efficient analog eigenbeamforming procedure for wideband mmwave mimo-ofdm systems," in *2022 IEEE 23rd International Symposium on a World of Wireless, Mobile and Multimedia Networks (WoWMoM)*, 2022, pp. 214–220.